Geophysical Journal International

Non-linear 3D Born Shear Waveform Tomography in Southeast Asia

Journal:	*Geophysical Journal International*
Manuscript ID:	GJI-11-0577.R1
Manuscript Type:	Research Paper
Date Submitted by the Author:	n/a
Complete List of Authors:	Panning, Mark; University of Florida, Department of Geological Sciences; Cao, Aimin; University of California, Berkeley, Berkeley Seismological Laboratory; TGS-NOPEC Geophysical, Kim, Ahyi; University of California, Berkeley, Berkeley Seismological Laboratory Romanowicz, Barbara; Berkeley Seismological Laboratory,
Keywords:	Asia < GEOGRAPHIC LOCATION, Tomography < GEOPHYSICAL METHODS, Seismic anisotropy < SEISMOLOGY, Surface waves and free oscillations < SEISMOLOGY

SCHOLARONE™
Manuscripts

For Review

submitted to *Geophys. J. Int.*

Non-linear 3D Born Shear Waveform Tomography in Southeast Asia

Mark P. Panning[1⋆], Aimin Cao[2,3], Ahyi Kim[2,4], and Barbara A. Romanowicz[2]

[1] *Department of Geological Sciences, University of Florida, Gainsville, FL* 32611*, USA*

E-mail: mpanning@ufl.edu

[2] *Berkeley Seismological Laboratory, University of California, Berkeley, Berkeley, CA* 94720*, USA*

[3] *now at TGS-NOPEC Geophysical, Houston, TX, USA*

[4] *now at Graduate School of Nanobioscience, Yokohama City University, Yokohama, Japan*

Received 2011 August 30; in original form 2011 August 30

For Peer Review

SUMMARY

Southeast (SE) Asia is a tectonically complex region surrounded by many active source regions, thus an ideal test bed for developments in seismic tomography. Much recent development in tomography has been based on 3D sensitivity kernels based on the first-order Born approximation, but there are potential problems with this approach when applied to waveform data. In this study, we develop a radially anisotropic model of SE Asia using long period multi-mode waveforms. We use a theoretical "cascade" approach, starting with a large-scale Eurasian model developed using 2D NACT sensitivity kernels, and then using a modified Born approximation (nBorn), shown to be more accurate at modeling waveforms, in order to invert a subset of the data for structure in a subregion (longitude 75° to 150° and latitude 0° to 45°). In this subregion, the model is parameterized at a spherical spline level 6 (∼200 km). The dataset is also inverted using NACT and purely linear 3D Born kernels. All 3 final models fit the data well, with just under 80% variance reduction as calculated using the corresponding theory, but the nBorn model shows more detailed structure than the NACT model throughout and has much better resolution at depths greater than 250 km. Based on variance analysis, the purely

linear Born kernels do not provide as good a fit to the data due to deviations from linearity for the waveform dataset used in this modeling. The nBorn isotropic model shows a stronger fast velocity anomaly beneath the Tibetan plateau in the depth range of 150 km to 250 km, which disappears at greater depth, consistent with other studies. It also indicates moderate thinning of the high velocity plate in the middle of Tibet, consistent with a model where Tibet is underplated by Indian lithosphere from the south and Eurasian lithosphere from the north, in contrast to a model with continuous underplating by Indian lithosphere across the entire plateau. The nBorn anisotropic model detects negative ξ anomalies suggestive of vertical deformation associated with subducted slabs and convergent zones at the Himalayan front and Tien Shan at depths near 150 km.

Key words: Asia – Tomography – Seismic anisotropy – Surface waves and free oscillations

1 INTRODUCTION

The western Pacific subduction zones and southeast (SE) Asia make up a very diverse and tectonically active part of the world. All aspects of plate tectonics can be studied there: old and young subduction zones, back-arc and intraplate volcanism, continental collision, and active sea floor spreading. Due to this active tectonic setting, many earthquakes are available to illuminate the structure, as well as many broadband seismic station (Fig. 1). This combination makes this region an ideal setting for testing out new approaches for seismic modeling with the goal of better understanding the tectonic history and ongoing dynamics of the region.

In this study, we develop a 3D radially anisotropic model of the upper mantle beneath SE Asia, using long period fundamental mode and overtone time domain surface waveforms. We utilize a theoretical "cascade" approach, where we first develop a large-scale Eurasian model using the well-developed theoretical framework of Non-linear Asymptotic Coupling Theory (NACT, Li & Romanowicz 1995), and then zoom in on a smaller region with a more targeted dataset using a new approach based on a modified 3D Born approach (nBorn, Panning et al. 2009) (see regions in Fig. 1). Including anisotropy is a first-order necessity when modeling a three component waveform

⋆ Author to whom correspondence should be addressed

For Peer Review

dataset, and the resulting anisotropic model provides constraints on mantle deformation processes beneath this region.

1.1 Previous Studies

Although SE Asia is seismically very active, the distribution of seismicity is restricted to the plate boundaries. Additionally the station distribution in much of this region is relatively sparse, without the addition of difficult to obtain Chinese data (e.g. Li et al. 2006). However, the P wave velocity structure beneath the western Pacific plate, Philippine sea and Indonesia has been extensively studied because of active seismicity in that region and dense station distribution (e.g. van der Hilst et al. 1991; Fukao et al. 1992; Obayashi & Fukao 1997; Widiyantoro & van der Hilst 1997; Nakajima et al. 2001).

Recently, Li et al. (2006, 2008) developed a P-wave velocity model in SE Asia using short period P travel time data from the International Seismological Centre (ISC) and from the Annual Bulletin of Chinese Earthquake (ABCE) which were not previously reported to ISC, as well as long period differential PP-P travel time data. In their model, they found a pronounced high velocity anomaly down to 300 km beneath the region of the Precambrian Indian continent. They also found Indian lithospheric mantle underthrust beneath the south eastern part of the Tibetan Plateau down to 400 km. A number of fundamental mode surface wave studies have also been conducted because low seismicity and relatively few stations in the continental region make many body wave methods impractical. In addition to many studies across Tibet (e.g. Romanowicz 1982; Griot et al. 1998; Rapine et al. 2003; Shapiro et al. 2004), these studies are frequently focused on the Philippine sea region (e.g. Seekins & Teng 1977; Oda & Senna 1994; Nakamura & Shibutani 1998). Lebedev & Nolet (2003) and Priestley et al. (2006) include higher-mode surface waves which greatly improves resolution in the upper mantle. Their studies also show the pronounced high-velocity continental roots beneath several Precambrian tectonic units of SE Asia. The SE asia region is also one focus of the larger Eurasian S velocity model of Kustowski et al. (2008), which was also able to image the Indian lithosphere subducting beneath Tibet. The depth to the base of the Indian lithosphere in this model was broadly consistent although somewhat deeper than that obtained using receiver

For Peer Review

functions (Kumar et al. 2006, 2007). This region has also served as the test bed for innovative theoretical approaches to seismic tomography, such as the model of Friederich (2003) developed using a full waveform dataset and sensitivity kernels based on multiple forward scattering.

2 METHODOLOGY

2.1 Theoretical approach

While many types of seismic data are used in tomographic modeling, such as absolute travel times, cross-correlation travel times, or surface wave phase delays, in this study we develop a new model of structure in SE Asia using full waveform tomography. Theoretical advances in forward modeling and calculation of sensitivity kernels have played a critical role in the development of waveform tomography. From the 1D path average approximation (PAVA) (Woodhouse & Dziewonski 1984), to the 2D approximation of non-linear asymptotic coupling theory (NACT) (Li & Romanowicz 1995), to 3D kernels based on the first-order Born approximation (e.g. Takeuchi 2007), the first order global mantle structures have been well revealed based on long period shear waveform inversions. Additionally, many innovative approaches take advantage of numerical wavefield computations for full waveform tomography on regional scales of crust (e.g. Chen et al. 2007; Tape et al. 2010) and mantle structure (e.g. Fichtner et al. 2010), as well as at the global scale (Lekić & Romanowicz 2011). However, it is important that the theoretical limitations of various approximations be systematically evaluated in order to understand how best to utilize waveform data to more accurately map short wavelength mantle structures (e.g. Romanowicz et al. 2008; Panning et al. 2009).

All of these methods have strengths and drawbacks. While the 3D Born approximation takes off-great circle plane scattering into account, PAVA and NACT approximations simply collapse the effect of 3D structure onto the 2D great circle plane. When seismic anomalies are weak with sizes larger than the first Fresnel zone, PAVA, NACT, and 3D Born all perform well for fundamental modes, although PAVA does not fit overtones well (Romanowicz et al. 2008). Because it brings out the ray character of body waves in a broadband sense, NACT improves the fit for overtones,

For Peer Review

but the improvement is greater for 3D Born. This suggests that the off-path anomalies also play a role in the waveforms of higher mode surface waves.

When anomalies are weak and smaller than the first Fresnel zone, neither PAVA nor NACT fit fundamental or overtone modes well because both approximations assume the anomaly is relatively constant over the Fresnel zone. In particular, in the case of a ray path passing immediately adjacent to the anomaly, both PAVA and NACT completely fail (Romanowicz et al. 2008; Panning et al. 2009). Only 3D Born can correctly predict the off-great circle effects. This illustrates how 3D Born kernels can improve the resolution of shorter wavelength structures.

Nonetheless, 3D Born breaks down for waveform modeling when an anomaly is strong and large relative to the reference model (Panning et al. 2009). In this case, the multiple forward scattered wave field is comparable in amplitude to that of the reference wavefield, and it is no longer appropriate to neglect the higher order terms during the linearization (Capdeville 2005). PAVA and NACT do not suffer the same breakdown because they consider the linear perturbation of phase of the waveform, rather than the total waveform, which is valid at long times and also includes some contribution from multiple forward scattering along the great circle (Friederich et al. 1993, appendix). One way to avoid the shortcoming of 3D Born is to utilize iterative numerical approaches so that, in particular, the 3D reference model can incorporate these large-scale anomalies *a priori* (e.g. Tape et al. 2010; Fichtner et al. 2010; Lekić & Romanowicz 2011). In the context of computationally less expensive normal mode-based approaches which rely on 1D reference models, Panning et al. (2009) introduced a modified non-linear Born approach (nBorn), by adding in higher order terms based on the path-average predicted phase delay. While it significantly improves the modeling of waveforms perturbed by large phase delay from long wavelength structure, nBorn can still correctly model the 3D sensitivity effects of shorter wavelength structures.

The nBorn approach can be briefly explained as modifying the linear single-scattering Born approximation with the addition of higher-order terms derived from PAVA. The first-order Born approximation simply assumes that waveforms through a modified Earth model can be calculated as a linear perturbation from waveforms calculated from a reference model, e.g.

$$\mathbf{u}_{\mathrm{Born}}(t) = \mathbf{u}_0(t) + \delta\mathbf{u}_{\mathrm{Born}}(t), \quad (1)$$

For Peer Review

where $\mathbf{u}_0$ is a reference trace which can be calculated, for example, from a mode sum,

$$\mathbf{u}_0(t) = \sum_{k=0}^{N} \mathbf{u}_k(t), \tag{2}$$

where N is the number of normal modes in the frequency band of interest, and $\mathbf{u}_k$ is defined as

$$\mathbf{u}_k(\Delta, t) = \mathbf{A}_k(\Delta)\cos(\omega_k t), \tag{3}$$

where Δ is the epicentral distance, ω_k is the eigenfrequency of the mode in the reference model, and $\mathbf{A}_k$ is an excitation and phase term related to the eigenfunctions at the source and receiver depths and generalized associated Legendre functions (Phinney & Burridge 1973) of the epicentral distance. The linear first-order Born perturbation, $\delta\mathbf{u}_{\mathrm{Born}}$, can be calculated with a variety of methods, but the normal mode-based approach used in the present study is detailed in Capdeville (2005).

On the other hand, PAVA, as introduced by Woodhouse & Dziewonski (1984), involves linear perturbations to the epicentral distance ($\delta\Delta$) and mode frequency ($\delta\hat{\omega}_k$), both of which act as an effective perturbation to the phase of the reference waveform,

$$\mathbf{u}_{\mathrm{PAVA}}(t) = \sum_{k} \mathbf{A}_k(\Delta + \delta\Delta)\cos\left[(\omega_k + \delta\hat{\omega}_k)t\right]. \tag{4}$$

The perturbations $\delta\Delta$ and $\delta\hat{\omega}_k$ are discussed in more detail in Woodhouse & Dziewonski (1984) and Panning et al. (2009). A linear perturbation in phase such as this acts as a non-linear perturbation to the waveform when the phase perturbations, $\delta\Delta$ and $\delta\hat{\omega}_k$, become large. Capturing this nonlinearity, not included in the first-order Born approximation, is essential for accurate modeling of waveforms over which large phase delays are accumulated (Panning et al. 2009).

The nBorn approach is based on the idea that the linear Born perturbation, $\delta\mathbf{u}_{\mathrm{Born}}$, contains the linear contribution from $\mathbf{u}_{\mathrm{PAVA}}$, as well as linear contributions from off-path scatterers, but not the higher-order non-linear waveform perturbations implicitly included in equation 4. The Born waveforms can therefore be improved if we add in only the higher-order PAVA terms, excluding the linear contribution, so that it is not counted twice. This is accomplished using a hybrid expression that adds the linear Born terms to the PAVA waveform with a linearized PAVA contribution removed,

$$\mathbf{u}(t) = \mathbf{u}_{\mathrm{PAVA}}(t) + \delta\mathbf{u}_{\mathrm{Born}}(t) - \delta\mathbf{u}_{\mathrm{PAVA}}(t), \tag{5}$$

For Peer Review

where $\delta\mathbf{u}_{\mathrm{PAVA}}$ is the linearized PAVA contribution, derived in Panning et al. (2009) as

$$\delta\mathbf{u}_{\mathrm{PAVA}} = \delta\Delta\mathbf{A}_k^{'}(\Delta)\cos(\omega_k t) - t\delta\hat{\omega}_k\mathbf{A}_k(\Delta)\sin(\omega_k t), \quad (6)$$

where $\mathbf{A}_k^{'} = \mathrm{d}\mathbf{A}_k/\mathrm{d}\Delta$ is the derivative of the excitation terms with respect to Δ.

Waveforms calculated using the nBorn expression (equation 5) do indeed show significant improvement relative to linear first-order Born predictions in synthetic testing (Panning et al. 2009), and only require minimal computation beyond the 3D linear Born kernels.

The 3D kernels do, however, involve significantly more computational costs than the well-developed 2D NACT approach. For this reason, we choose to begin the modeling of this region using a cascade approach where a large-region model is first developed using a global dataset, and then further modeling is done using nBorn kernels on a smaller subregion using a subset of the full global dataset.

2.2 Data and Model Parameterization

The global dataset used in the development of the initial large region Eurasian NACT model consists of 3 component fundamental and overtone surface waveforms, recorded at global broad band stations from the IRIS global seismographic network (GSN) and the Geoscope global network, for events at teleseismic and far regional distances (15° – 165°). Most of the dataset was assembled for previous global (Mégnin & Romanowicz 2000; Panning & Romanowicz 2006) and regional (Marone et al. 2007) tomographic studies. We utilize all paths from this dataset that cross the large region of interest. In this study, to make path coverage more homogeneous, we also collected additional events, which occurred in southeastern Africa in the period 2001-2004.

Each seismogram has been deconvolved and filtered between 60s and 400s. Individual fundamental and higher mode first orbit energy packets have been extracted using an automated selection algorithm (Panning & Romanowicz 2006) which compares the data with synthetics calculated for the reference velocity model PREM (Dziewonski & Anderson 1981). Subsequently the selected datasets are checked by hand, to ensure a final high quality dataset. The windowing method which we applied allows a weighting scheme that prevents larger amplitude phases from dominating the inversion, thus balancing, in particular, contributions from the fundamental mode

For Peer Review

and overtones. Additional weighting is implemented to account for redundancy of certain paths (Li & Romanowicz 1996, Appendix A). The magnitude of earthquakes which were used in the inversion is restricted from M_W 6 to M_W 7 to avoid noisy data and complicated source-time functions. The source parameter information is obtained from the CMT (Centroid Moment Tensor) catalog (http://www.globalcmt.org). After the waveform selection, we obtained 15,377 fundamental mode and 25,376 overtone wave packets from 482 events, which provide fairly dense path and homogeneous azimuthal coverage (fig. 2A).

For the second modeling step, we limited the data used to the 162 events in the catalog that occurred within the large region used in the first modeling step. Additionally we only used data recorded in the 52 broadband stations contained within the large region (fig. 1). This reduced the total number of wavepackets to 3628, but path density remains good in the smaller subregion of the modeling in the second step (fig. 2B).

The model is parameterized as a radially anisotropic medium, which can be described with 5 independent elastic coefficients (A, C, F, L, N) (Love 1927). We used an equivalent parametrization in terms of Voigt average isotropic S and P velocity (Babuska & Cara 1991), and three anisotropic parameters ξ, ϕ and η. We inverted for V_S and ξ, using scaling factors derived from Montagner & Anderson (1989) to constrain the other 3 independent parameters that cannot be resolved from the inversion of long period waveforms.

In the initial step, we develop a large-scale Eurasian model (from longitude 30^o to 150^o, and latitude 10^o South to 60^o North) using the large global dataset and NACT theory for the sensitivity kernel calculation. Structure outside the region of interest is fixed to that of SAW642AN (Panning & Romanowicz 2006), and all perturbations are relative to the 1D reference model PREM (Dziewonski & Anderson 1981). The large region NACT model is parametrized for the isotropic and for the radial anisotropic structure in level 6 and 5 spherical splines (Wang & Dahlen 1995), respectively (fig. 3A and B). At level 6, the knots are $\sim$2^o apart and at level 5, knots are $\sim$4^o apart. In depth, the model is parametrized in terms of cubic splines (Mégnin & Romanowicz 2000), which are distributed irregularly in depth in the upper mantle and down to 100 km, reflecting the irregular distribution of data sensitivity with depth, with finer knot spacing in the shallower depth range.

For Peer Review

The knot locations for this model correspond to the top 10 knots of the Mégnin & Romanowicz (2000) study. Outside of this region, the fixed structure of SAW642AN is parameterized in level 4 splines for both V_S and ξ, as in the original version of the model (Panning & Romanowicz 2006).

In the final step, we use multiple theories to invert for a model in a smaller region focused more on southeast Asia, outlined in figure 1 (longitude 75^o to 150^o and latitude 0^o to 45^o). This model is parameterized with level 6 splines for both V_S and ξ, with structure outside this subregion fixed to the starting NACT model described in the preceding paragraph. We limit the radial sampling to the top 5 knots of Mégnin & Romanowicz (2000), which provides sampling down to 470 km.

In both steps, crustal structure is corrected linearly with NACT for the topography/bathymetry and Moho topography of CRUST2.0 (Bassin et al. 2000). This correction is performed by calculating linear sensitivity kernels relative to PREM, the starting 1D model. Certainly, multiple studies have indicated linear crustal corrections such as this are likely inadequate (e.g. Marone & Romanowicz 2007; Lekić et al. 2010), and may have significant influence on recovered structure, particularly in anisotropic structure (Ferreira et al. 2010; Panning et al. 2010). This is very important to keep in mind when interpreting the final models; however, the main thrust of this research comparing the influence of multiple theories on the recovered models simply requires consistent crustal corrections across all models, and therefore simple linear corrections were considered adequate.

3 RESULTS

In the initial step, we perform 3 inversion iterations using NACT to produce a large continental-scale Eurasian model of V_S (fig. 4) and ξ (fig. 5). The goal of this step is to obtain a higher-resolution starting model for the nBorn modeling than the level 4 splines of the global SAW642AN model, which only provides sampling at a node spacing of $\sim$8 degrees. The resulting model improves the fit to the surface wave dataset with a final variance reduction of 68% calculated across the whole dataset (i.e. the residual variance as estimated by the squared residuals of data minus synthetics is only 32% of the summed squared amplitude of the original data).

With this starting model in place, we proceed to the second step, which is to produce an nBorn-

For Peer Review

derived model for the smaller subregion (fig. 1). Because the calculation of the 3D Born sensitivity kernels is much more expensive computationally, we also limit the dataset to a subset of paths that are entirely contained in the larger region of step 1, as already discussed in section 2.2. In order to better evaluate improvement in modeling using the nBorn approach, we also use this same reduced dataset to invert for an NACT model in the subregion, as well as an inversion using the purely linear Born kernels, without the nBorn modification of Panning et al. (2009). Three model iterations are performed for each of the three modeling approaches. This allows for a more direct comparison between models developed using an identical dataset, but with three different theoretical approaches.

For the nBorn model, 3D Born kernels are calculated inside the region, and are modified to include the non-linear PAVA part according to Panning et al. (2009). Outside of the subregion, we use NACT to compute the contribution to synthetics, and structure is held fixed to the starting model. For the NACT inversion in the subregion, we use the NACT method to compute the contribution to synthetics both inside and outside the region, and invert using NACT kernels calculated within the subregion. Finally, for the linear Born model, we use only the linear 3D kernels inside the subregion, while still using NACT to account for the structure outside the subregion. The adopted damping scheme for isotropic and radially anisotropic models is the same as that used in our large region model developed in step 1, although we do explore the residual variance as a function of the overall damping amplitude to determine our final damping choice (see section 4). In all 3 models, we use linear NACT-based crustal corrections based on CRUST2.0, consistent with that used in construction of the starting model.

First, we compare the shear velocity nBorn model with the NACT and linear Born models in the depth range of 60 km to 400 km (fig. 6 and 7). In the shallow upper mantle the nBorn and the NACT models agree well, while the linear Born model shows more different structure. At the depth of 60 km the high velocity in the Indian plate and the low velocity beneath the Tibetan Plateau, Tarim Basin, and the back-arc basins of the Pacific plate and the Philippine plate show a good match between the nBorn and the NACT model, while the low velocity anomaly below Tibet is mostly absent in the linear Born model (fig. 6). At a depth of 150 km, all 3 models show simi-

For Peer Review

lar large-scale structure. Edges of structures, however, are visibly sharper in the nBorn and Born models, with smaller scale features present, such as a localized low velocity anomaly at depth beneath the Tarim Basin. At a depth of 250 km, the nBorn model shows somewhat higher velocity beneath the eastern Tibetan Plateau, reaching into the Sichuan Basin, although all three models show high velocities beneath Tibet for the depth range between 150 and 250 km, possibly arguing against lithospheric delamination as a mechanism for uplift of the plateau. The most striking difference between the models is found at depths larger than 300 km (fig. 7). While the NACT model shows relatively constant structure with depth without clear correlation to surface tectonics, depth-dependent structure remains apparent in the nBorn and Born models (fig. 7). In particular, these models show clear high velocity anomalies associated with Pacific subduction zones as well as a shift from high velocities beneath the Tibetan Plateau at a depth of 250 km towards lower velocity anomalies at depths greater than 300 km.

Second, we compare the anisotropic portion of the models for the three theories in the depth range of 60 km to 400 km (fig. 8 and 9). Radial anisotropy, which assumes a vertical axis of symmetry needs to be introduced when simultaneously modeling Love and Rayleigh wave data. We use the parameter $\xi = V_{SH}^2/V_{SV}^2$ to describe this anisotropy in this model. Regions where $\xi > 1$ thus indicate $V_{SH} > V_{SV}$, while negative perturbations indicate $V_{SV} > V_{SH}$. Because the observation of anisotropy by seismic waves requires large-scale alignment of either crystallographic axes (lattice-preferred orientation, or LPO) or regions of contrasting elastic properties (shape-preferred orientation, or SPO), 3D variations of anisotropy can be an important tool to identify either dynamic flow processes in many depth ranges in the mantle or frozen-in structures at lithospheric depths. Under the assumption of dominant A-type and E-type olivine fabric development (e.g. Karato et al. 2008; Long & Becker 2010), we would expect horizontal flow to lead to $V_{SH} > V_{SV}$, or $\xi > 1$, while more vertical flow would lead to $V_{SV} > V_{SH}$, or $\xi < 1$, allowing us to interpret 3D variations of radial anisotropy in terms of dominant horizontal vs. vertical flow. Above the depth of 250 km, we plot the perturbations from PREM in fig. 8, but it is important to note that the PREM reference model (Dziewonski & Anderson 1981) includes radial anisotropy above 220 km decreasing linearly from $\sim$10% at the moho (meaning $V_{SH} > V_{SV}$) to zero at a depth of 220 km. This

For Peer Review

means that even the relatively strong red features shown at depths of 60 and 150 km actually just represent relatively weak $V_{SH} > V_{SV}$ anisotropy in most regions, rather than $V_{SV} > V_{SH}$ (fig. 10). In other words, the nBorn and the NACT models basically inherit the intrinsic anisotropic feature in the reference 1D model PREM. In the lithosphere, however, $V_{SH} > V_{SV}$ remains the dominant feature. At a depth of 60 km, the NACT and nBorn models are quite similar, while the Born model shows stronger differences (fig 8). Most notably, it has the opposite sign in the region stretching from the Tarim Basin to the Sichuan Basin, to the north of the Tibetan Plateau. It is important to note, however, that this is a region with strong variation in crustal thickness while we are using linear crustal corrections, and previous studies have demonstrated that crustal corrections can have an important influence, particularly on anisotropic structure (Marone & Romanowicz 2007; Ferreira et al. 2010; Panning et al. 2010), making interpretation difficult. Along the subduction zones of the Pacific and the Philippine plates, all three models show the downwellings as zones of negative ξ perturbations associated with the subducted slabs at a depth of 150 km, although the anomalies are more sharply defined in the nBorn and Born models. At the Tien Shan converging zone and the Himalayan front, we also show a similar negative ξ signal. The nBorn and Born models show a contrasting region of positive ξ perturbations beneath the Tibetan Plateau at a depth of 150 km, which may relate to some sort of horizontal flow beneath Tibet in this depth range (e.g. underplating of Indian and/or Eurasian lithosphere), although interpretations remain limited by concerns about crustal corrections. In the depth range of 300 km to 400 km, the NACT model shows little change in the anisotropic structures as in the isotropic portion of the model, while the nBorn and Born models reveals slightly more detailed anisotropic structures, although they are not clearly correlated with regional tectonic activities (fig. 9).

Third, we compare three profiles (fig. 11 and 12) in the three models in the tectonically interesting region of the Tibetan Plateau and Himalayan front. While all 3 models show apparent subducted Indian plate in all three velocity profiles, we note that the nBorn and Born models show a transition at depth from positive to negative velocity anomalies. These models appear to image the bottom of the Indian plate lithosphere much more clearly. Also, in profile CD, we note a moderate thinning of the high velocity plate in the middle of Tibet, consistent with the result of Friederich

For Peer Review

(2003), suggesting a model where Tibet is underplated by Indian lithosphere from the south and Eurasian lithosphere from the north (e.g. Tapponnier et al. 2001), in contrast to a model with continuous underplating by Indian lithosphere across the entire plateau. This is also consistent with results from early studies indicating poor Sn propagation through north central Tibet (Barazangi & Ni 1982), and the possible absence of a lithospheric lid (Brandon & Romanowicz 1986; Bourjot & Romanowicz 1992). Recent receiver function results also favor this scenario (Kumar et al. 2006).

We also show a cross-section in the well-sampled portion of the model covering some of the western Pacific subduction zones. Profile GH (fig. 13), across the Japan subduction zone, which is usually fairly visible in global models in the uppermost mantle, shows up very clearly in the nBorn model. The NACT model also shows fast velocities associated with the slab, but it is less clearly delineated due to the poorer resolution at depth. The linear Born model also outlines the slab, but appears less continuous than the nBorn model.

The large differences in structure at depth between the models developed with different theories are reflected in checkerboard resolution testing. This testing is performed using resolution matrices calculated from the last model iteration inversion for each theoretical approach. It therefore evaluates resolution due to the source-receiver geometry of the dataset, the choice of damping, and the geographic coverage of each methods' sensitivity kernels, but does not evaluate the influence of noise in the data or incorrect theoretical assumptions. We perform checkerboard resolution tests using a two layer model for V_S with a shallow 4 degree checkerboard and a deep 8 degree pattern (fig. 14). For ξ, we also use two layers with alternating 8 degree checkerboards (fig. 15). At a shallow depth the resolution is sharp throughout the isotropic model in the Born and nBorn models, while significant smearing is present in the NACT model. Resolution is poorer at depth in all three models, but is once again much sharper in the nBorn and Born models, particularly in the region of densest coverage in the southeast portion of the model. The anisotropic structure is not resolved as well as the isotropic structure, but is still generally well-resolved at shallow depths in the nBorn and Born models. Amplitudes are strongly reduced in all three models at depth, with the NACT model showing virtually zero resolution of anisotropic structure at depth. A test with larger wavelength 12 degree squares is also presented in the supplementary material as figures S1

For Peer Review

and S2. All three models generally show good recovery of this structure in V_S although with amplitude reduction in ξ, particularly at depths greater than 200 km, and amplitudes are lower in the NACT model in comparison to the 3D kernel models with less sharp transitions. At these longer wavelengths, the ξ resolution maps look very similar to the 8 degree patterns.

4 DISCUSSION

With the theoretical underpinnings of the three approaches (Panning et al. 2009), we might expect that shorter-wavelength features would be preferentially imaged in the nBorn and Born models, while the purely linear Born modeling may present problems in the inversion when dealing with large, high-amplitude anomalies. Indeed, qualitatively, the nBorn and Born models appear to have sharper features than the NACT model. In the shallowest part of the model, where the amplitude anomalies are the highest, the linear Born model shows a different structure from the nBorn and NACT models in the longest wavelength anomalies, although the nBorn does share many similarities with the linear Born model in the shorter wavelength features, particularly in the eastern portion of the model. This possibly indicates the shortcomings of the purely linear theory, which the modified nBorn kernels avoid. In the deeper part of the model, resolution testing clearly indicates that the 3D approaches have superior resolution, and the resulting models appear to have more reasonable tectonic correlations for depths greater than 200 km. Of course, such qualitative comparisons do not rigorously determine whether any particular model is better than another.

The obvious first step in analyzing the relative merits of different models is to compare the data fit in each case, as calculated within the corresponding theory. All 3 models can fit waveforms very well, with up to $\sim$80 percent variance reduction (depending on the choice of damping) (fig. 16). Of course, determining variance reduction relies on both the details of the model and the forward theory used to calculate synthetics through that model. In order to address this issue, we chose to calculate variance reduction for all three models using synthetics calculated with each of the three different theoretical approaches. Variance reduction also strongly depends on choice of damping, se we also chose to explore a range of overall damping for each model. We chose to develop a suite of models, consisting of 6 models for each theoretical approach, resulting from using an overall

For Peer Review

damping parameter that we varied over five orders of magnitude. We then calculated synthetics through each of these 18 models using each of the three theoretical approaches in order to calculate data fit as weighted residual variance,

$$\sigma_r^2 = \frac{\sum_{i=0}^{N} w_i (d_i - s_i)^2}{\sum_{i=0}^{N} w_i d_i^2}, \tag{7}$$

where N is the number of data points, d_i and s_i are the data and synthetic respectively, and w_i is the weighting for each data point in the inversion. These values are displayed graphically in figure 16, where low residual variance indicates better overall fit to the data.

When the same theory is used for both the model inversion and the forward variance calculation, we note similar behavior for all three models (solid line in top panel, dashed line in middle panel, and dash-dotted line in bottom panel in fig. 16). This is not terribly surprising, of course, as the inverse approach is fundamentally designed to improve the fit as measured by the theory used to construct the sensitivity kernels. These curves follow the typical pattern with improved data fit with lower damping levels, but with decreasing marginal benefit as the damping levels become low. As usual, a compromise damping choice needs to be made that provides optimal data fit, while discouraging spurious structure in the resulting model. For the models displayed in this study, a value of 5×10^{-5} was used for all 3 models, providing a nominal variance reduction of 78.6%, 77.0% and 73.9% for the NACT, nBorn and Born models, respectively, when the same theory is used for both inversion and variance calculation. We note, however, that the nBorn and Born models do not show the same degree of flattening at low damping levels as the NACT model. This is qualitative evidence that less damping may be required with 3D kernels, analogous to more quantitative studies such as Boschi et al. (2006) which suggested, via the use of the Akaike Information Criterion, that the use of Born kernels in the context of global surface wave phase velocity maps allowed for models with marginally more effective model parameters than ray-theoretical approaches. This study differs in that we are modeling waveforms, and comparing theories that all are nominally "finite-frequency," but the Born and nBorn kernels represent 3D sensitivity, while NACT is limited to the 2D great-circle plane.

It is also interesting to compare how well each model fits the data when the forward calculations are done with a different theoretical approach than that used in the inversion. Some interest-

For Peer Review

ing patterns emerge from this. First, variance calculated with the linear Born theory is generally higher than that calculated using the other two approaches, even for some of the linear Born-derived models. This is a fairly clear manifestation of the problem with the use of the linear Born approach in waveform modeling identified in Panning et al. (2009). In these models for the period range of these waveforms, perturbations are large enough that linearity is not always warranted and therefore the fit degrades. Secondly, it is worthwhile to note that the nBorn models (fig. 16, bottom panel) show a consistent pattern for all three methods of calculating the variance, where decreasing damping leads to improved data fit. The fit is the best when the nBorn theory is used for variance calculation, as expected, but the same pattern at slightly higher variances is observed when the variance is calculated with either linear Born or NACT as well. For the NACT models, on the other hand, a different behavior is apparent (fig. 16, middle panel). At the lowest levels of damping, the variance as calculated via nBorn or Born actually starts to increase with decreased damping.

This can likely be understood by considering that, to first order, all of the NACT sensitivity is included in the kernels for the nBorn model. Models which obtain a good fit to data using nBorn calculations should therefore also provide good fit using NACT instead. However, the NACT kernels do not have the off-path sensitivity that the nBorn kernels provide. For models with relatively large amplitude and shorter wavelength features (as are typical of models with lower damping), these off-path effects become more important. Because such sensitivity is not included in the NACT sensitivity kernels, underdamped models do not result in improved fits when variance is calculated with the nBorn theory. This feature has potentially interesting implications for methods that intend to take advantage of more advanced forward calculations in an inverse approach while using simpler kernels in the inversion. While it is more important to compute the misfit using an accurate theory, in order to have a chance to converge to the right solution, while kernels can be computed approximately (e.g. Lekić & Romanowicz 2011), it is important to damp the inversion adequately, which may result in more numerous iterations. Note that this is not a complete comparison with that approach, as all of the inversions performed in this study did use a consistent theory when calculating the misfit for use in the inversion. The comparison here just used differ-

For Peer Review

ent theories to calculate the data fit in the final inverted models. The Born models also show a somewhat similar signature, where the NACT-derived variances start to increase with decreasing damping at the low damping end. This may be another symptom of the breakdown of linearity in larger-amplitude models.

It is also important to consider the effect of regularization in this inversion. For comparison, all models in this paper are shown with the same values of regularization used for all three models. However, since the methods have different derivatives to populate the inversion, the effects of regularization will not necessarily be identical. Since we are able to calculate the resolution matrix of this model, we can quantify this by looking at the trace of the resolution matrix, which can be considered a measure of the effective number of model parameters in the inversion. Of course all 3 models share the same number of model parameters, but regularization leads to correlations between model parameters which reduce the effective number of unknowns. While all of these models have 7600 model parameters within the subregion of interest, the trace of the resolution matrix varies from 566.5 for the NACT model, to 805.2 for the modified Born model, to 858.4 for the linear Born model. This implies that the regularization has a larger impact on the NACT inversion, which may lead to some of the differences we see, possibly particularly at greater depths where the NACT model shows little depth variation, and the resolution tests suggest amplitudes are not well recovered. In order to test this, we also plot an NACT model with the overall damping parameter set to 2×10^{-5}, which produces a resolution matrix with a trace of 852.5, comparable to the nBorn and Born models at the higher damping level. We then recreate figures 6 to 9 as supplementary figures S3-S6 comparing the less-damped NACT model to the nBorn and Born models already shown. In V_S, the patterns of structure in the NACT model remain virtually unchanged, with a correlation across the model coefficients in the subregion above 0.94 for all depths between 25 and 400 km, although the amplitude is increased. The correlation also remains high in the ξ structure, remaining above 0.91 in the same depth range, although once again, the amplitudes are larger. This strongly suggests regularization alone is not responsible for the differences in the three models.

Given the overall similar variance reduction numbers for the three models, it is not a simple

For Peer Review

problem to statistically determine which model should be preferred. Model fit to the data depends on choices of damping and theoretical choices for the misfit calculation, and it is therefore not trivial to determine which values to use in any standard statistical test, such as the F-test. However, there are qualitative reasons to prefer the nBorn model in this experiment. At shallow depths, large-scale, high-amplitude velocity perturbations produce large enough phase delays that the linearity of the Born waveform kernels is violated, and there is reason to question the validity of the modeling using only the linear kernels. And in this depth range, we indeed see the nBorn model diverges from the linear Born model in the uppermost 100 km of the model (fig. 17). While correlation between the nBorn and Born models, as calculated across the model coefficients in the region of interest, is generally near 0.9 over most of the depth range, it dips between 0.6 and 0.7 in the shallowest part of the model in both V_S and ξ. In this same depth range, the NACT and Born models are very different with correlations dipping to 0.1 in V_S and becoming slightly anti-correlated in ξ. The nBorn model, on the other hand clearly has characteristics from both models with similar correlation to both NACT and linear Born models. Given the insight from forward modeling (Panning et al. 2009), as well as from visual inspection (fig. 6), this is a strong suggestion that the hybrid approach is accurately modeling the longer wavelength structure present in the NACT model due to the additional non-linear terms, while still modeling the shorter-wavelength structure present in the linear Born model. For structure at greater depths, however, model perturbations are smaller, and therefore the linear Born kernels may be expected to perform better. Resolution testing also suggests significant advantages for the 3D kernels at these greater depths relative to NACT for this particular dataset. At this depth range, the nBorn model is more similar to the linear Born model and diverges from the NACT model, which shows relatively constant structure with depth with no obvious relationship to known tectonics. This is good qualitative evidence that the hybrid nBorn approach is reaping the advantages of the linear Born kernels in areas where NACT does not perform well, while still maintaining the advantages of the use of linear phase perturbations in NACT for regions where the linear Born approximation breaks down. In order to better evaluate this claim quantitatively, future work may suggest the use of more exact numerical calculations to evaluate misfit, although such approaches are always complicated by the influence of the crust on

For Peer Review

real data. Fully synthetic tests with the data coverage of this study, but using a known or simplified crustal structure are another possibility, but are outside the scope of the current study.

5 CONCLUSION

The systematic comparison of the nBorn and the NACT models shows that the newly developed normal mode-based approximation nBorn has the capability to image more detailed structures in the upper mantle than NACT for this surface waveform dataset, while analysis of estimates of residual data variance suggest the method also performs better than purely linear Born kernels for waveforms in this frequency range. The models illuminate several features of regional tectonics, including the isotropic signature of subducted lithosphere beneath Tibet. This lithosphere shows evidence of moderate thinning below the platform possibly supportive of a model of combined subduction from India to the south and Eurasia to the north rather than continuous Indian underplating, but does not show any obvious evidence of lithospheric delamination. Anisotropic signatures in the model suggest negative ξ perturbations possibly relating to vertical deformation in the 150 km depth range beneath the western Pacific subduction zones as well as the Himalayan front and the Tien Shan converging zone. Investigation of variance reduction calculated with the different theories suggests less damping may be required for inversions using 3D kernels, and also suggests that caution is needed to avoid underdamping and ensure convergence when using a simpler theory for the calculation of inversion kernels than for the forward calculation of data misfit.

For Peer Review

A C K N O W L E D G M E N T S

All figures were made using GMT (Wessel & Smith 1998). MP was supported through NSF grant EAR-0911414. The linear Born kernels were calculated using a code written by Y. Capdeville. The manuscript benefited from comments from J. Trampert, L. Boschi and an anonymous reviewer.

REFERENCES

Babuska, V. & Cara, M., 1991. *Seismic Anisotropy in the Earth*, Kluwer Academic Press, Boston, Massachusetts.

Barazangi, M. & Ni, J., 1982. Velocities and propagation characteristics of Pn and Sn beneath the Himalayan arc and Tibetan plateau: Possible evidence for underthrusting of the Indian continental lithosphere beneath Tibet, *Geology*, **10**, 179–185.

Bassin, C., Laske, G. & Masters, G., 2000. The current limits of resolution for surface wave tomography in north america, *EOS Trans. Amer. Geophys. Union*, **81**, F897.

Boschi, L., Becker, T., Soldati, G. & Dziewonski, A., 2006. On the relevance of Born theory in global seismic tomography, *Geophys. Res. Lett.*, **33**, L06302, doi:10.1029/2005GL025063.

Bourjot, L. & Romanowicz, B., 1992. Crust and upper mantle tomography in Tibet using surface-waves, *Geophys. Res. Lett.*, **19**, 881–884.

Brandon, C. & Romanowicz, B., 1986. A "no-lid" zone in the central Chang-Thang platform of Tibet: Evidence from pure path phase velocity measurements of long period Rayleigh waves, *J. Geophys. Res.*, **91**(B6), 6547–6564.

Capdeville, Y., 2005. An efficient Born normal mode method to compute sensitivity kernels and synthetic seismograms in the earth, *Geophys. J. Int.*, **163**(2), 639–646.

Chen, P., Zhao, L. & Jordan, T., 2007. Full 3D tomography for the crustal structure of the Los Angeles region, *Bull. Seism. Soc. Amer.*, **97**(4), 1094–1120.

Dziewonski, A. & Anderson, D., 1981. Preliminary Reference Earth Model, *Phys. Earth Planet. Inter.*, **25**, 297–356.

Ferreira, A., Woodhouse, J., Visser, K. & Trampert, J., 2010. On the robustness of global radially anisotropic surface wave tomography, *J. Geophys. Res.*, **115**, doi:10.1029/2009JB006716.

Fichtner, A., Kennett, B., Igel, H. & Bunge, H.-P., 2010. Full waveform tomography for radially anisotropic structure: New insights into present and past states of the Australasian upper mantle, *Earth Planet. Sci. Lett.*, **290**, 270–280.

Friederich, W., 2003. The S-velocity structure of the east Asian mantle from inversion of shear and surface waveforms, *Geophys. J. Int.*, **153**, 88–102.

Friederich, W., Wielandt, E. & Strange, S., 1993. Multiple forward scattering of surface waves: comparison with an exact solution and Born single-scatternig methods, *Geophys. J. Int.*, **112**, 264–275.

Fukao, Y., Obayashi, M., Inoue, H. & Nenbai, M., 1992. Subducting slabs stagnant in the mantle transition zone, *J. Geophys. Res.*, **97**(B4), 4809–4822.

Griot, D., Montagner, J.-P. & Tapponnier, P., 1998. Confrontation of mantle seismic anisotropy with two extreme models of strain in Central Asia, *Geophys. Res. Lett.*, **25**, 1447–1450.

Karato, S.-I., Jung, H., Katayama, I. & Skemer, P., 2008. Geodynamic significance of seismic anisotropy

For Peer Review

of the upper mantle: New insights from laboratory studies, *Annu. Rev. Earth Planet. Sci.*, **36**, 59–95.

Kumar, P., Yuan, X., Kind, R. & Ni, J., 2006. Imaging the colliding Indian and Asian lithospheric plates beneath Tibet, *J. Geophys. Res.*, **111**, doi:10.1029/2005JB003930.

Kumar, P., Yuan, X., Kumar, M., Kind, R., Li, X. & Chadha, R., 2007. The rapid drift of the Indian tectonic plate, *Nature*, **449**, 894–897.

Kustowski, B., Ekström, G. & Dziewoński, A., 2008. The shear-wave velocity structure in the upper mantle beneath Eurasia, *Geophys. J. Int.*, **174**, 978–992.

Lebedev, S. & Nolet, G., 2003. Upper mantle beneath Southeast Asia from S velocity tomography, *J. Geophys. Res.*, **108**, 2048, doi:10.1029/2000JB000073.

Lekić, V. & Romanowicz, B., 2011. Inferring upper mantle structure by full waveform tomography with the Spectral Element Method, *Geophys. J. Int.*, **185**, 799–831.

Lekić, V., Panning, M. & Romanowicz, B., 2010. A simple method for improving crustal corrections in waveform tomography, *Geophys. J. Int.*, **182**(1), 265–278.

Li, C., van der Hilst, R. & Toksöz, M., 2006. Constraining P-wave velocity variation in the upper mantle beneath Southeast Asia, *Phys. Earth Planet. Inter.*, **154**, 180–195.

Li, C., van der Hilst, R., Meltzer, A. & Engdahl, E., 2008. Subduction of the Indian lithosphere beneath the Tibetan Plateau and Burma, *Earth Planet. Sci. Lett.*, **274**, 157–168.

Li, X.-D. & Romanowicz, B., 1995. Comparison of global waveform inversions with and without considering cross-branch modal coupling, *Geophys. J. Int.*, **121**, 695–709.

Li, X.-D. & Romanowicz, B., 1996. Global mantle shear velocity model developed using nonlinear asymptotic coupling theory, *J. Geophys. Res.*, **101**(B10), 22245–22272.

Long, M. & Becker, T., 2010. Mantle dynamics and seismic anisotropy, *Earth Planet. Sci. Lett.*, **297**, 341–354.

Love, A., 1927. *A Treatise on the Mathematical Theory of Elasticity*, Cambridge Univ. Press, Cambridge, U.K.

Marone, F. & Romanowicz, B., 2007. Non-linear crustal correction in high-resolution regional waveform seismic tomography, *Geophys. J. Int.*, **170**(1), 460–467.

Marone, F., Gung, Y. & Romanowicz, B., 2007. Three-dimensional radial anisotropic structure of the North American upper mantle from inversion of surface waveform data, *Geophys. J. Int.*, **170**, 460–467.

Mégnin, C. & Romanowicz, B., 2000. The 3D shear velocity structure of the mantle from the inversion of body, surface, and higher mode waveforms, *Geophys. J. Int.*, **143**, 709–728.

Montagner, J.-P. & Anderson, D., 1989. Petrological constraints on seismic anisotropy, *Phys. Earth Planet. Inter.*, **54**, 82–105.

Nakajima, J., Matsuzawa, T., Hasegawa, A. & Zhao, D., 2001. Three-dimensional structure of Vp, Vs, and Vp/Vs beneath northeastern Japan: Implications for arc magmatism and fluids, *J. Geophys. Res.*, **106**,

For Peer Review

21843–21857.

Nakamura, Y. & Shibutani, T., 1998. Three-dimensional shear wave velocity structure in the upper mantle beneath the Philippine sea region, *Earth Planets Space*, **50**, 939–952.

Obayashi, M. & Fukao, Y., 1997. P and PcP travel time tomography for the core-mantle boundary, *J. Geophys. Res.*, **102**, 17825–17841.

Oda, H. & Senna, N., 1994. Regional variation in surface wave group velocities in the Philippine Sea, *Tectonophysics*, **233**, 265–277.

Panning, M. & Romanowicz, B., 2006. A three-dimensional radially anisotropic model of shear velocity in the whole mantle, *Geophys. J. Int.*, **167**, 361–379.

Panning, M., Capdeville, Y. & Romanowicz, B., 2009. Seismic waveform modelling in a 3-D Earth using the Born approximation: potential shortcomings and a remedy, *Geophys. J. Int.*, **177**, 161–178.

Panning, M., Lekić, V. & Romanowicz, B., 2010. The importance of crustal corrections in the development of a new global model of radial anisotropy, *J. Geophys. Res.*, **115**, doi:10.1029/2010JB007520.

Phinney, R. & Burridge, R., 1973. Representation of the elastic-gravitational excitation of a spherical earth model by generalized spherical harmonics, *Geophys. J. R. astr. Soc.*, **34**, 451–487.

Priestley, K., Debayle, E., McKenzie, D. & Pilidou, S., 2006. Upper mantle structure of eastern Asia from multimode surface waveform tomography, *J. Geophys. Res.*, **111**, B10304, doi:10.1029/2005JB004082.

Rapine, R., Tilmann, F., West, M., Ni, J. & Rodgers, A., 2003. Crustal structure of northern and southern Tibet from surface wave dispersion analysis, *J. Geophys. Res.*, **108**, 2120, doi:10.1029/2001JB000445.

Romanowicz, B., 1982. Constraints on the structure of the Tibet Plateau from pure path phase velocities of Love and Rayleigh waves, *J. Geophys. Res.*, **87**, 6865–6883.

Romanowicz, B., Panning, M., Gung, Y. & Capdeville, Y., 2008. On the computation of long period seismograms in a 3D Earth using normal mode based approximations, *Geophys. J. Int.*, **175**(2), 520–536.

Seekins, L. & Teng, T., 1977. Lateral variations in the structure of the Philippine Sea plate, *J. Geophys. Res.*, **82**, 317–324.

Shapiro, N., Ritzwoller, M., Molnar, P. & Levin, V., 2004. Thinning and flow of Tibetan crust constrained by seismic anisotropy, *Science*, **305**, 233–236.

Takeuchi, N., 2007. Whole mantle SH velocity model constrained by waveform inversion based on three-dimensional Born kernels, *Geophys. J. Int.*, **169**, 1153–1163.

Tape, C., Liu, Q., Maggi, A. & Tromp, J., 2010. Seismic tomography of the southern California crust based on spectral-element and adjoint methods, *Geophys. J. Int.*, **180**, 433–462.

Tapponnier, P., Xu, Z., Roger, F., Meyer, B., Arnaud, N., Wittlinger, G. & Yang, J., 2001. Oblique stepwise rise and growth of the Tibet Plateau, *Science*, **294**, 1671–1677.

van der Hilst, R., Engdahl, R., Spakman, W. & Nolet, G., 1991. Tomographic imaging of subducted lithosphere below northwest Pacific islands arcs, *Nature*, **353**, 37–43.

For Peer Review

Wang, Z. & Dahlen, F., 1995. Spherical-spline parameterization of three-dimensional Earth models, *Geophys. Res. Lett.*, **22**(22), 3099–3102.

Wessel, P. & Smith, W., 1998. New, improved version of Generic Mapping Tools released, *EOS Trans. Amer. Geophys. Union*, **79**, 579.

Widiyantoro, S. & van der Hilst, R., 1997. Mantle structure beneath Indonesia inferred from high-resolution tomographic imaging, *Geophys. J. Int.*, **130**, 167–182.

Woodhouse, J. & Dziewonski, A., 1984. Mapping the upper mantle: Three dimensional modeling of Earth structure by inversion of seismic waveforms, *J. Geophys. Res.*, **89**, 5953–5986.

For Peer Review

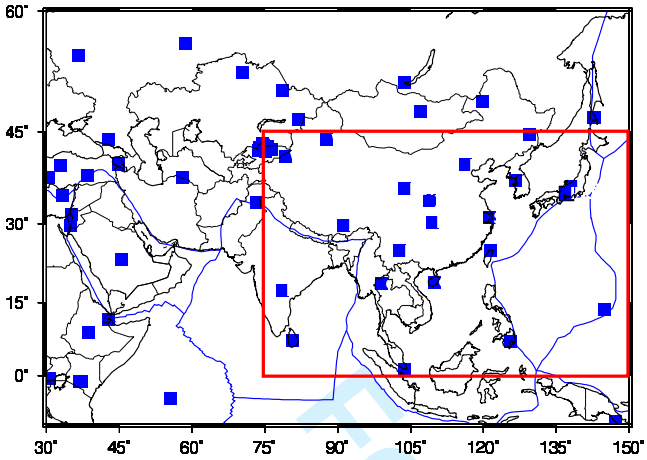

Figure 1. The subregion for both nBorn and NACT inversions in this study, which is outlined in the red rectangle (longitude 75^o to 150^o and latitude 0^o to 45^o). The large region shows the area of our starting NACT model (longitude 30^o to 150^o and latitude -10^o to 60^o). Also shown are the 52 broadband stations in the region (blue square) for which data was used in this study.

For Peer Review

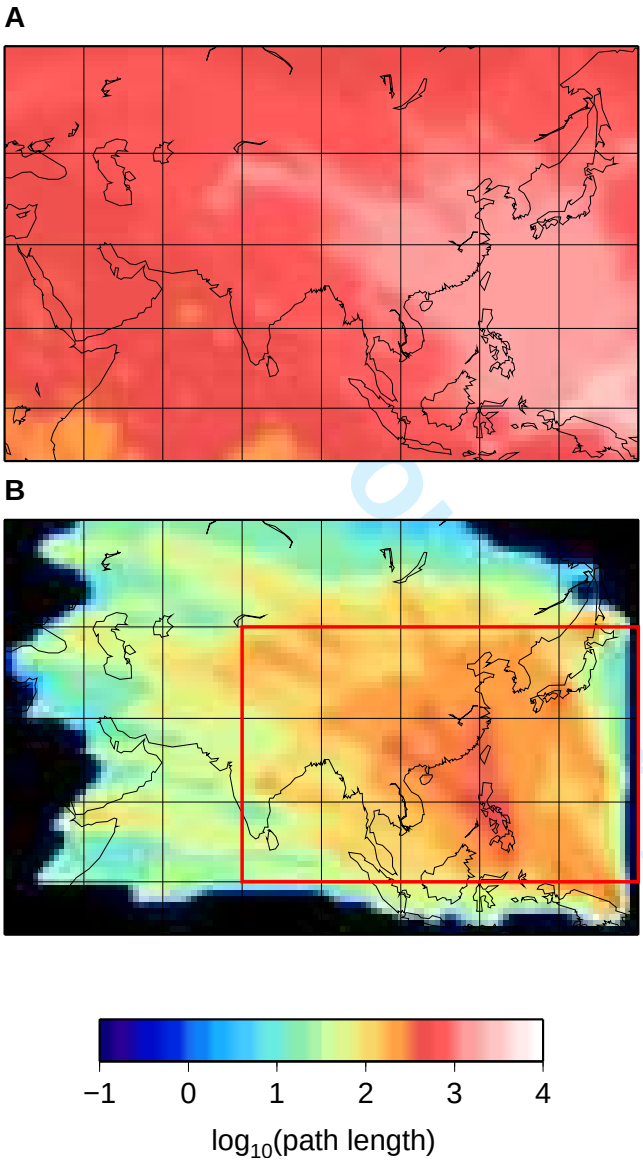

Figure 2. Raypath density coverage for the dataset used for the large region model (A) and the subset of the data used for the smaller region modeling in the second step (B). Color scale corresponds to the logarithm of summed path lengths (in degrees) crossing a 2^o by 2^o grid, approximating the sampling of the level 6 spline parameterization. The red square in (B) outlines the region for the smaller step 2 model, while the full map area in both panels is the region of interest for the large NACT starting model.

For Review

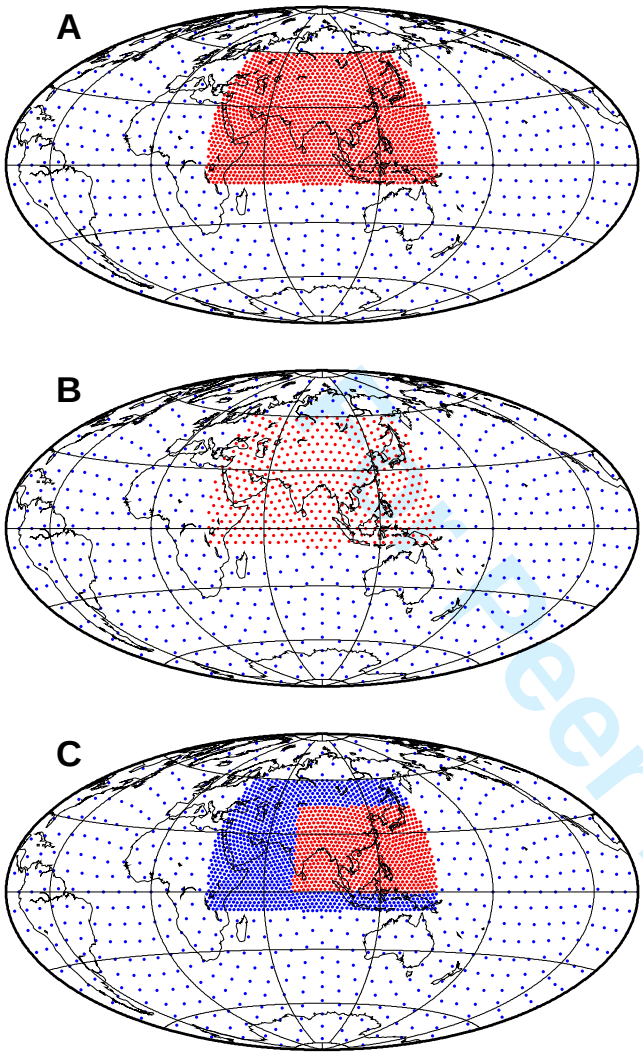

Figure 3. Spherical spline knot locations used in this study. (A) The meshing for large region isotropic V_S model is shown at spherical spline level 6 ($\sim$ 200 km) (red dots), with the blue dots representing the level 4 ($\sim$800 km) sampling of the starting model, SAW642AN (Panning & Romanowicz 2006), outside the region, which is held fixed in the inversion. (B) The ξ portion of the large region model is at spherical spline level 5 ($\sim$ 400 km) (red dots). (C) Inversion in the subregion using nBorn with both V_S and ξ at level 6 (red dots), and with structure fixed to the large region model outside of the subregion (blue dots).

For Peer Review

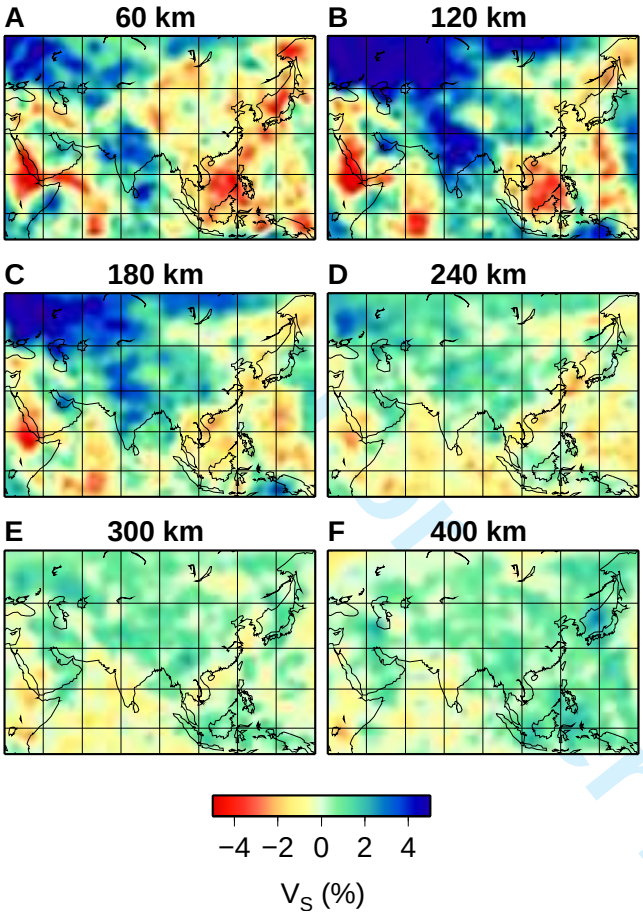

Figure 4. V_S structure from 60 km to 400 km depth in the large region NACT model. Perturbations are plotted relative to PREM.

For Peer Review

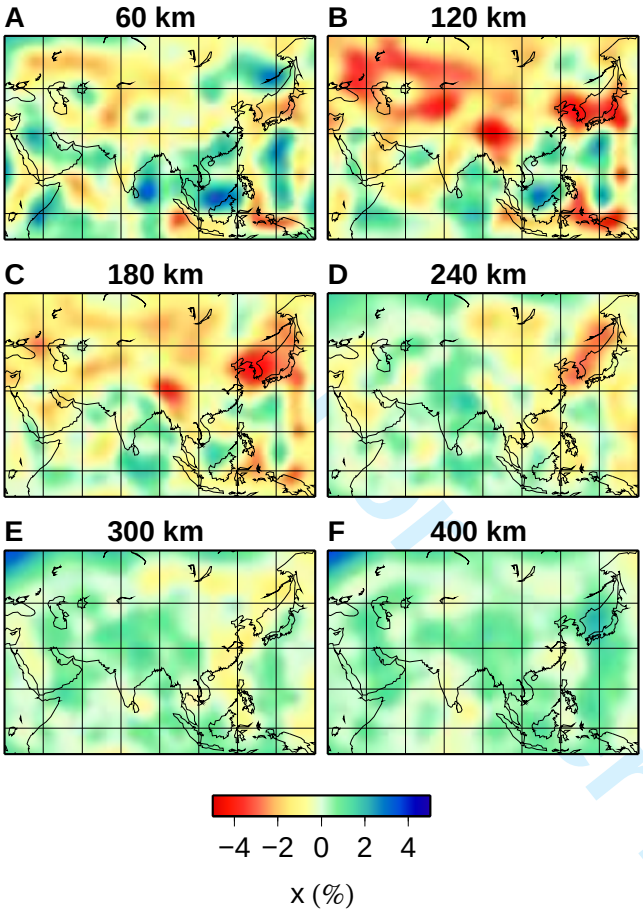

Figure 5. ξ structure from 60 km to 400 km depth in the large region NACT model. Perturbations are plotted relative to PREM. Note that PREM includes a linear gradient in $\xi = V_{SH}^2/V_{SV}^2$ from 1.1 ($V_{SH} > V_{SV}$) at the Moho back to 1.0 (isotropic) at 220 km depth.

For Peer Review

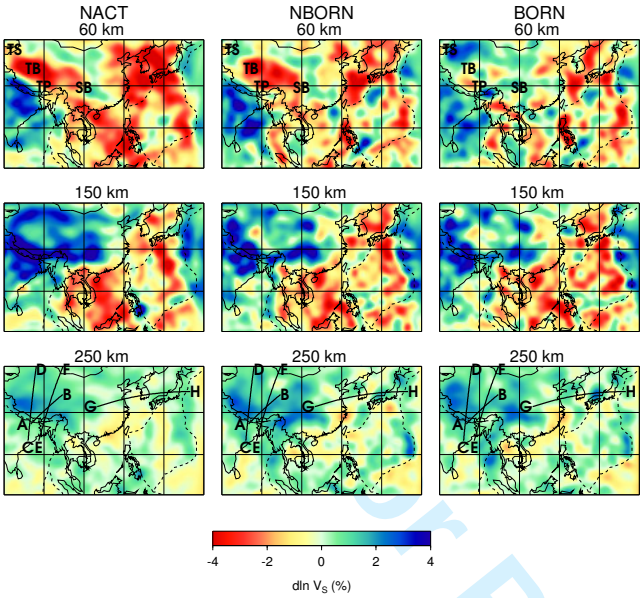

Figure 6. Comparison between NACT (left panels), nBorn (middle panels) and linear Born (right panels) shear isotropic models in the depth range of 60 to 250 km. TS, TB, TP, and SB denote Tien Shan, Tarim Basin, Tibetan Plateau, and Sichuan Basin, respectively. The lines labeled AB, CD, and EF in this and figure 7 correspond to the cross-sections in figures 11, 12 and 13. Profile AB is from (85^o, 26^o) to (97^o, 36^o), profile CD is from (88^o, 20^o) to (100^o, 45^o), profile EF is from (84^o, 20^o) to (88^o, 50^o), and profile GH is from (110^o, 32^o) to (145^o, 37^o).

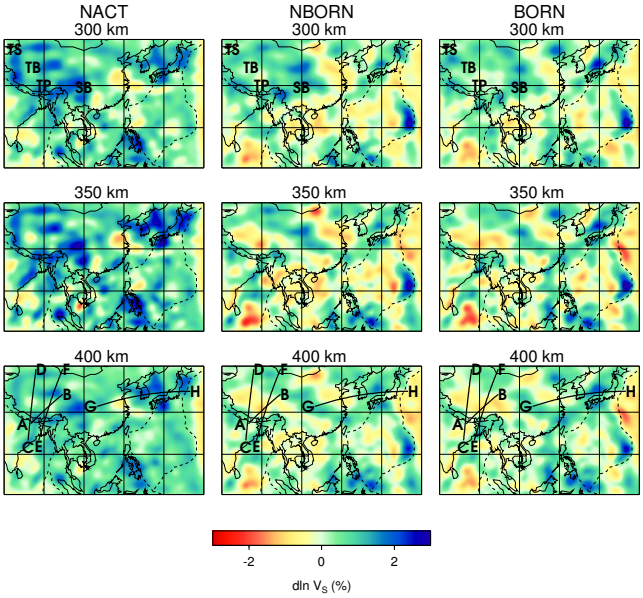

Figure 7. Same as figure 6 for the depth range from 300 to 400 km.

For Peer Review

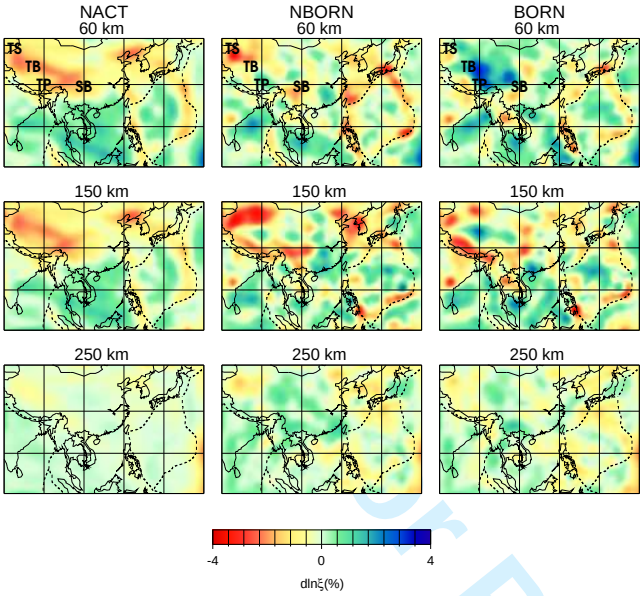

Figure 8. Comparison between NACT (left panels), nBorn (middle panels) and linear Born (right panels) anisotropic models in the depth range of 60 to 250 km. Geographic labels are the same as figure 6.

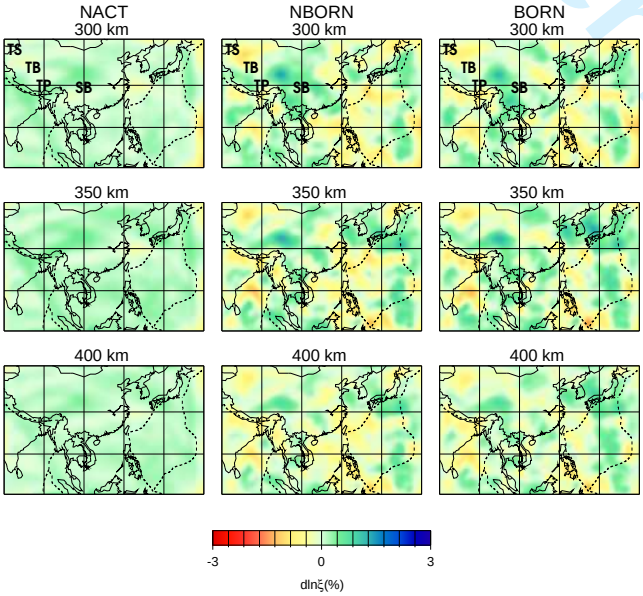

Figure 9. Same as figure 8 for the depth range from 300 to 400 km.

For Peer Review

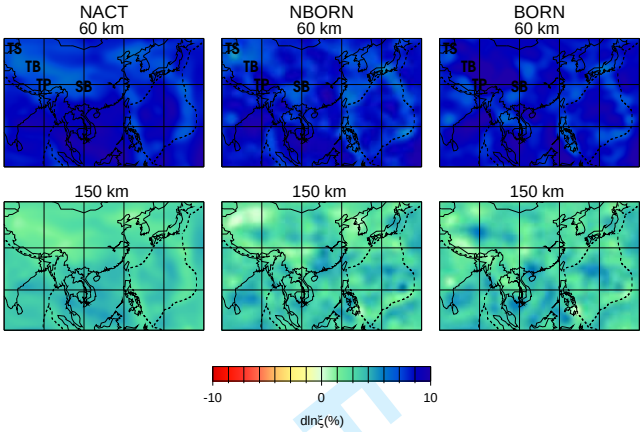

Figure 10. NACT (left panels), nBorn (middle panels) and linear Born (right panels) anisotropic models at depths of 60 (top) and 150 km (bottom). Perturbations are plotted relative to an isotropic model, and the structure includes the 1D anisotropic structure of PREM.

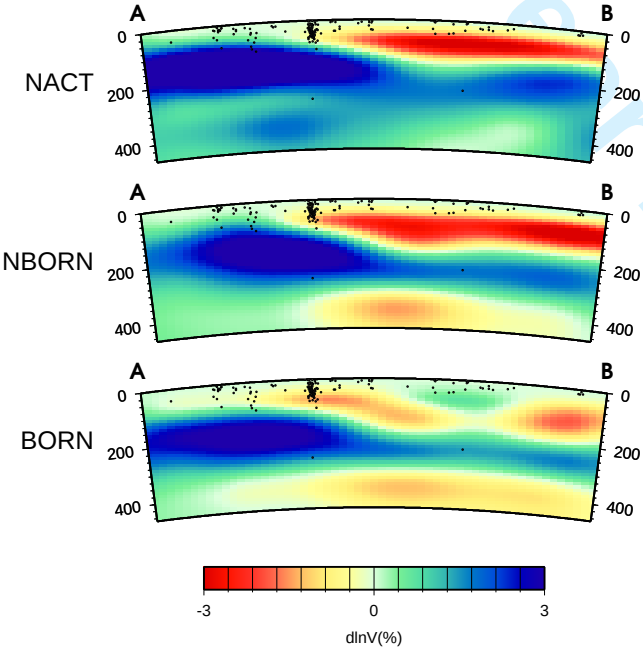

Figure 11. Profile AB from (85^o, 26^o) to (97^o, 36^o) (see figure 6). This profile corresponds to the profile DD' of Kustowski et al. (2008). Black dots are earthquake locations from a global catalog.

For Peer Review

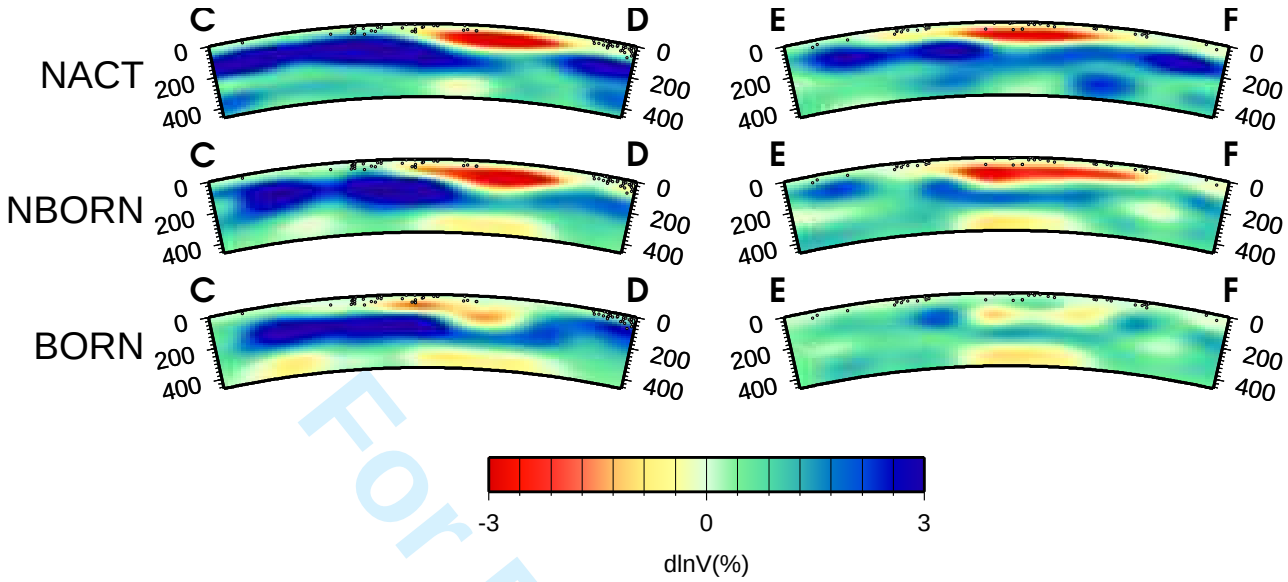

Figure 12. Profile CD from (88^o, 20^o) to (100^o, 45^o) and Profile EF from (84^o, 20^o) to (88^o, 50^o) (see figure 6). These correspond to the profiles A and B of *Friederich* (2003).

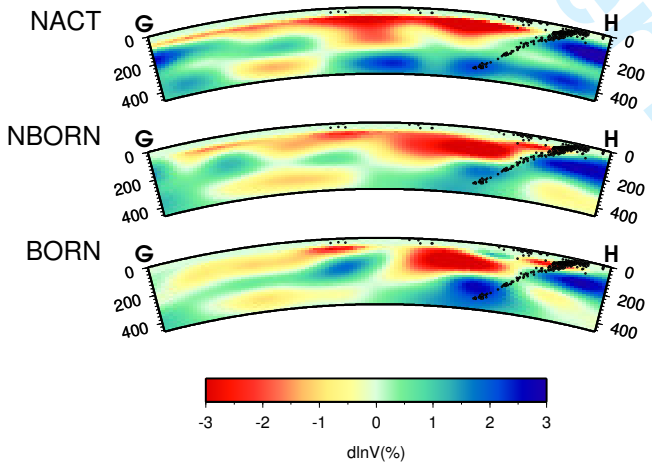

Figure 13. Profile GH from (110^o, 32^o) to (145^o, 37^o), cutting through the Japan slab.

For Peer Review

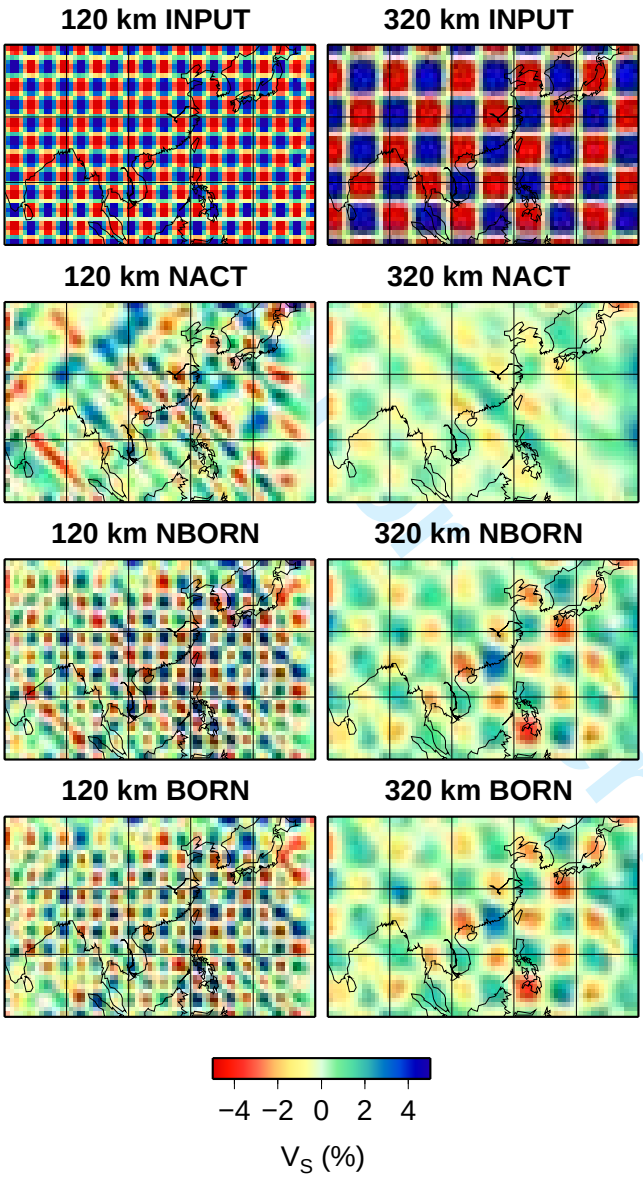

Figure 14. Resolution test of isotropic V_S. The input model consists of two layers of structure with peak amplitudes at 120 km (left panels) and 320 km (right panels). The input model is displayed in the top row, while the output for the NACT, nBorn, and linear Born inversion resolution tests are displayed in the following rows.

For Peer Review

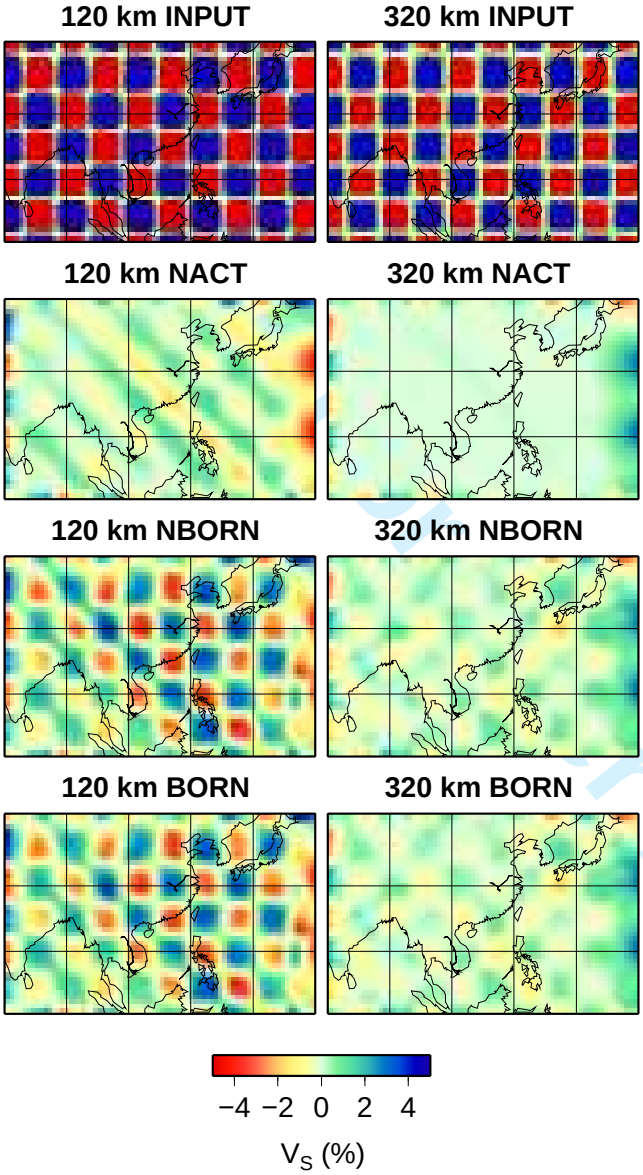

Figure 15. Same as figure 14 for an input ξ model.

For Review

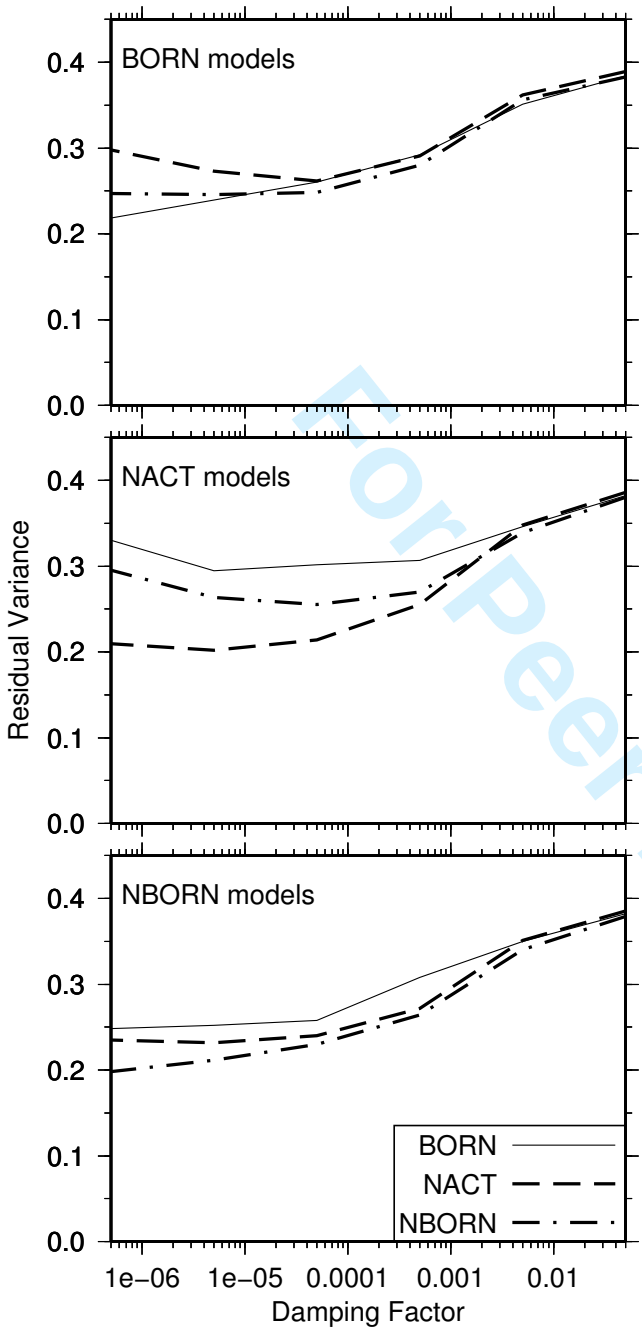

Figure 16. Residual variance versus the damping factor. Each panel plots residual variance (calculation described in text) on the y-axis against the value of the overall damping parameter along the x-axis. Residual variance is calculated for models developed from inversions using linear Born kernels (top), NACT kernels (middle), and nBorn kernels (bottom). In each set of models, residual variance is calculated using synthetics calculated using linear Born (solid line), NACT (dashed line) and nBorn theory (dash-dotted line).

For Peer Review

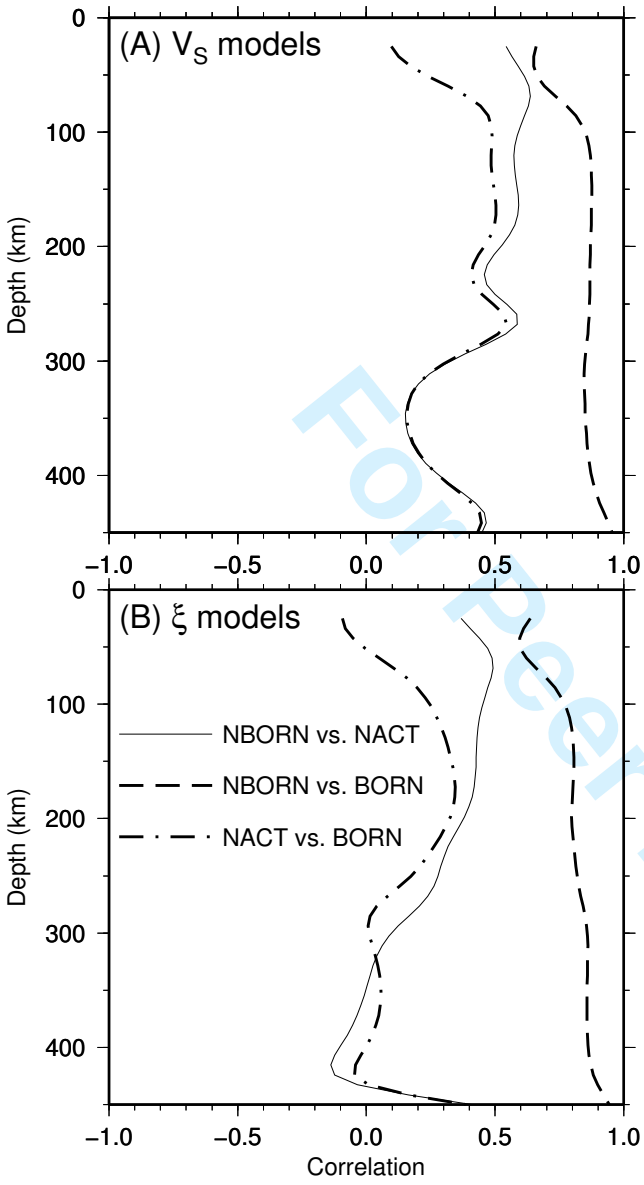

Figure 17. Correlation of V_S (A) and ξ models (B) as a function of depth over the coefficients in the subregion. Correlations are calculated between nBorn and NACT models (solid line), nBorn and linear Born models (dashed line), and NACT and linear Born models (dash-dotted line)

For Peer Review

submitted to *Geophys. J. Int.*

Non-linear 3D Born Shear Waveform Tomography in Southeast Asia - Supplementary material

Mark P. Panning[1⋆], Aimin Cao[2,3], Ahyi Kim[2,4], and Barbara A. Romanowicz[2]

[1] *Department of Geological Sciences, University of Florida, Gainsville, FL* 32611*, USA*

E-mail: mpanning@ufl.edu

[2] *Berkeley Seismological Laboratory, University of California, Berkeley, Berkeley, CA* 94720*, USA*

[3] *now at TGS-NOPEC Geophysical, Houston, TX, USA*

[4] *now at Graduate School of Nanobioscience, Yokohama City University, Yokohama, Japan*

Received 2011 August 30; in original form 2011 August 30

For Peer Review

1 SUMMARY OF SUPPLEMENTARY MATERIAL

Supplementary material for this paper includes 6 figures. Figures S1 and S2 are resolution matrix test output for models with large wavelength (12 degree) checkers for V_S and ξ, respectively. Figures S3-S6 are the same as figures 6-9 in the main article, but with a less-damped NACT model, which gives a comparable number of estimated model parameters (as estimated from the trace of the resolution matrix) as the Born and nBorn models.

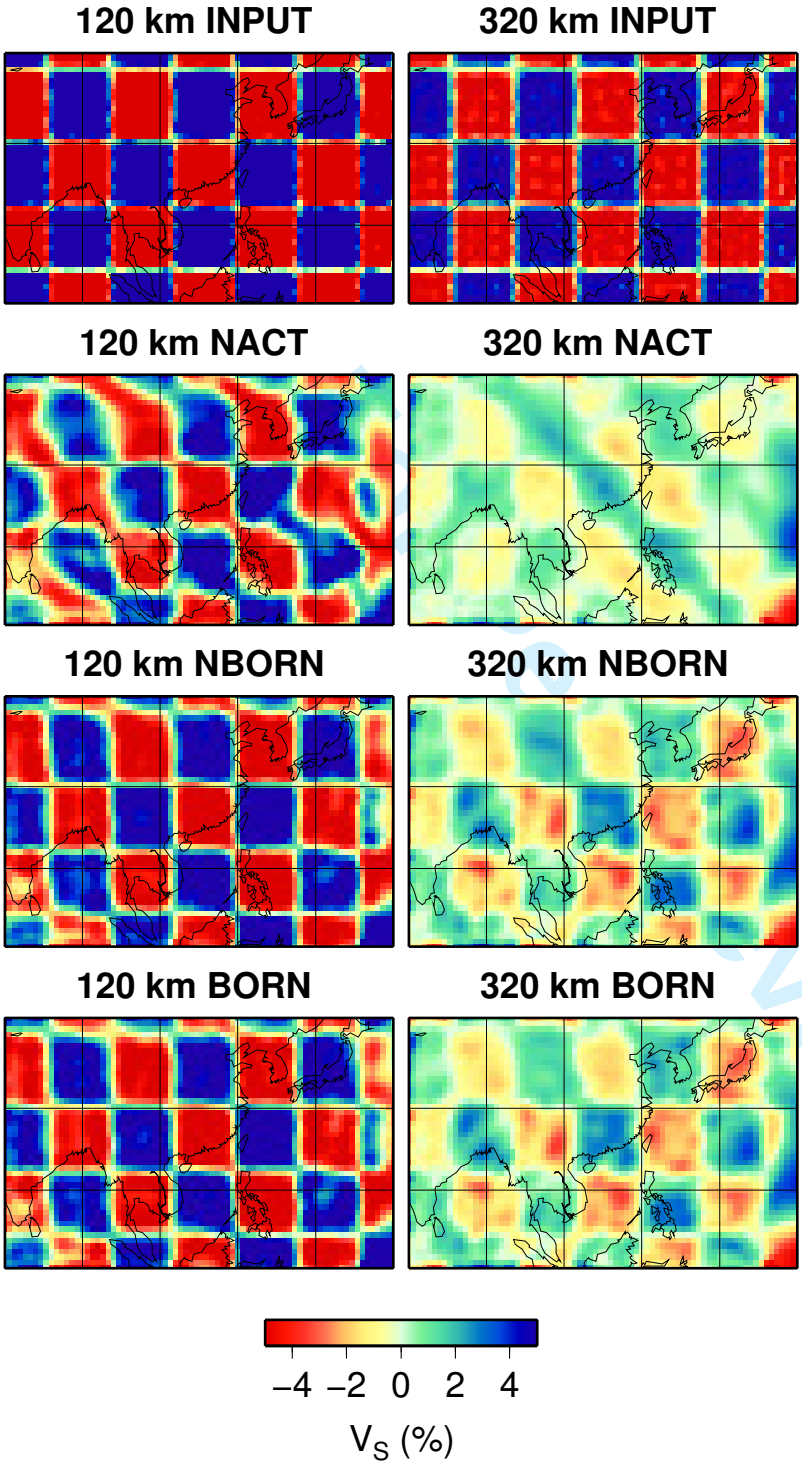

Figure S1. Resolution test of isotropic V_S. The input model consists of two layers of structure with 12 degree checkers with peak amplitudes at 120 km (left panels) and 320 km (right panels). The input model is displayed in the top row, while the output for the NACT, nBorn, and linear Born inversion resolution tests are displayed in the following rows.

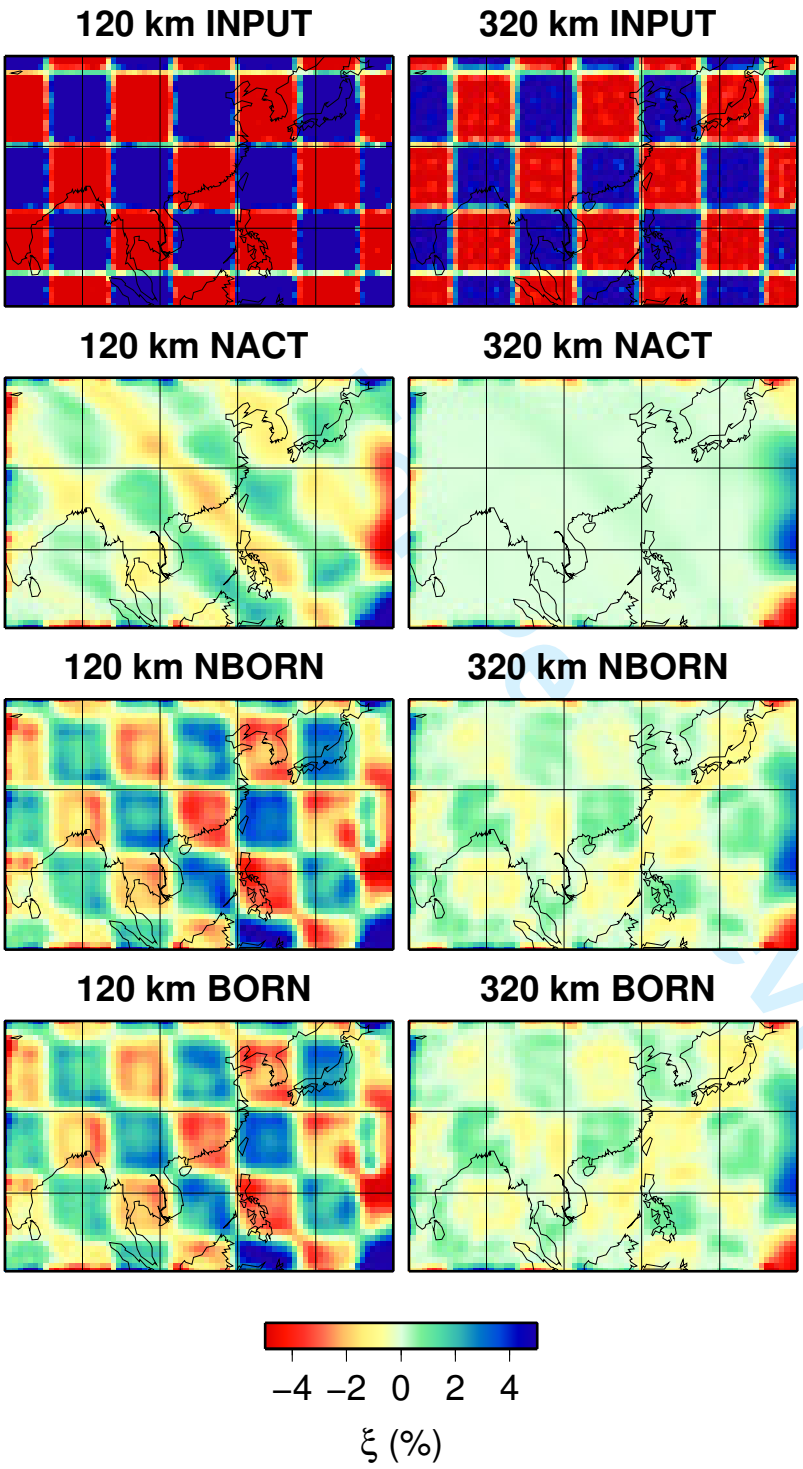

Figure S2. Same as figure S1 for ξ.

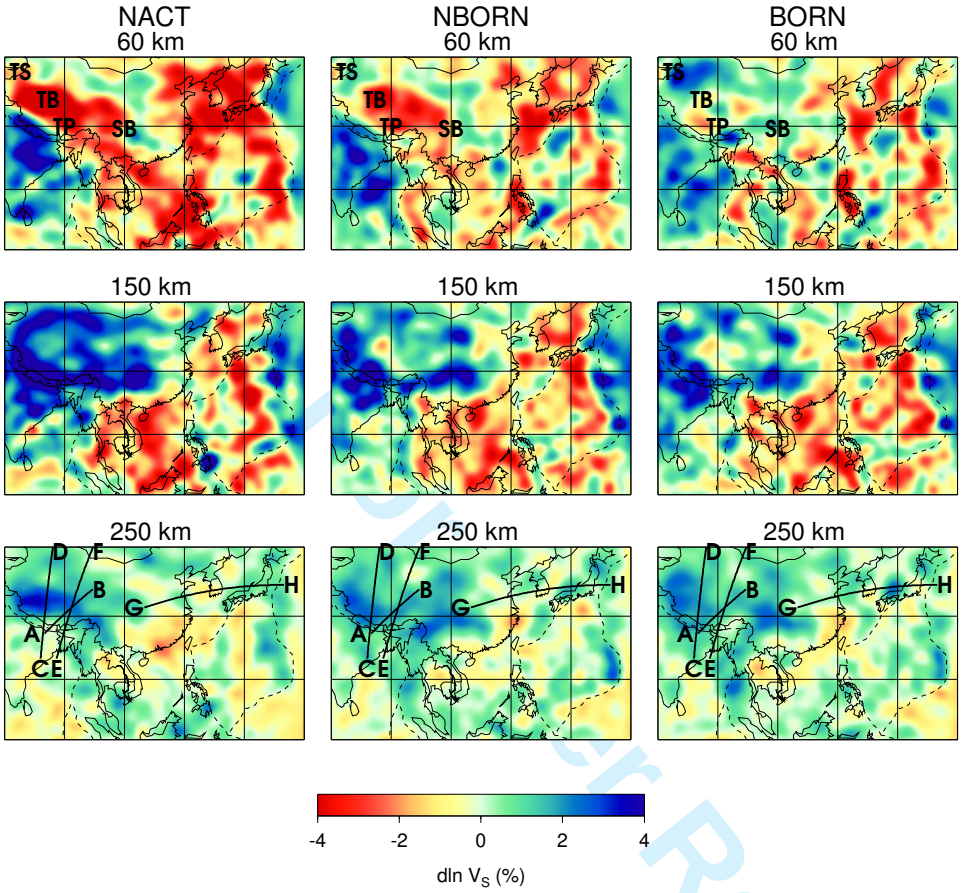

Figure S3. Comparison between NACT (left panels), nBorn (middle panels) and linear Born (right panels) shear isotropic models in the depth range of 60 to 250 km. TS, TB, TP, and SB denote Tien Shan, Tarim Basin, Tibetan Plateau, and Sichuan Basin, respectively. The lines labeled AB, CD, and EF in this and figure S4 correspond to the cross-sections in figures 11-13 in the article. The NACT model differs from the one displayed in figure 6 in the article by being less-damped, giving equivalent effective model parameters to the nBorn and linear Born models.

For Peer Review

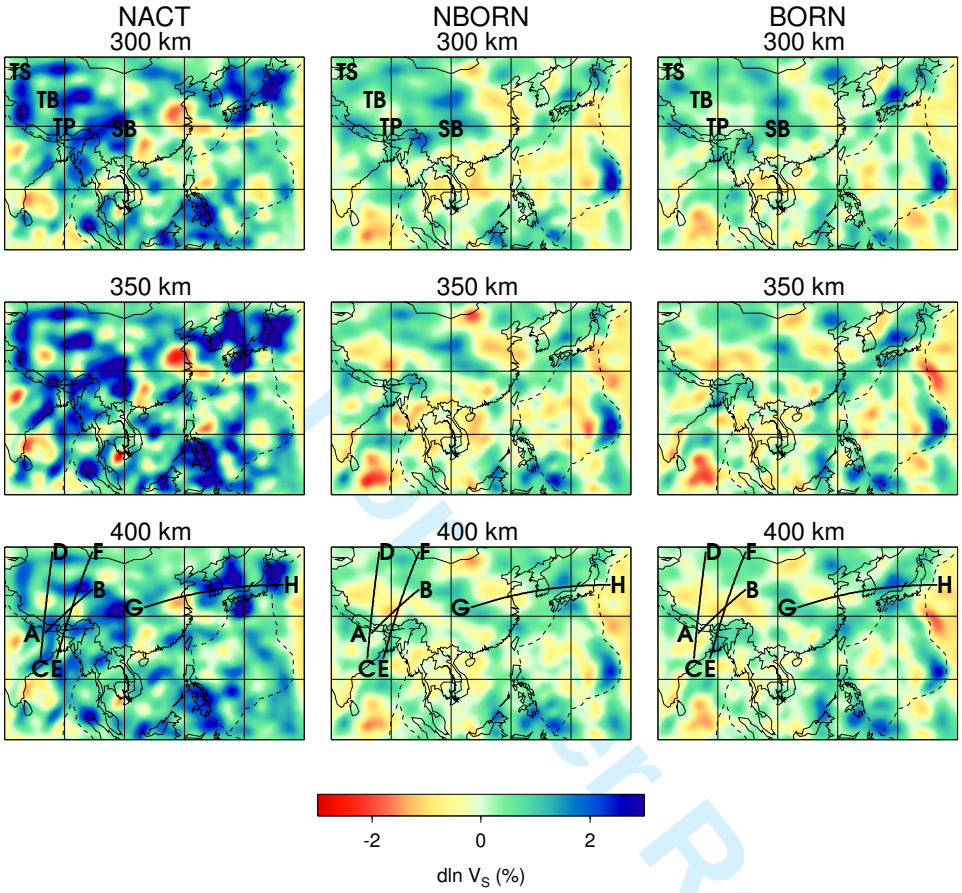

Figure S4. Same as figure S3 for depths between 300 and 400 km.

For Peer Review

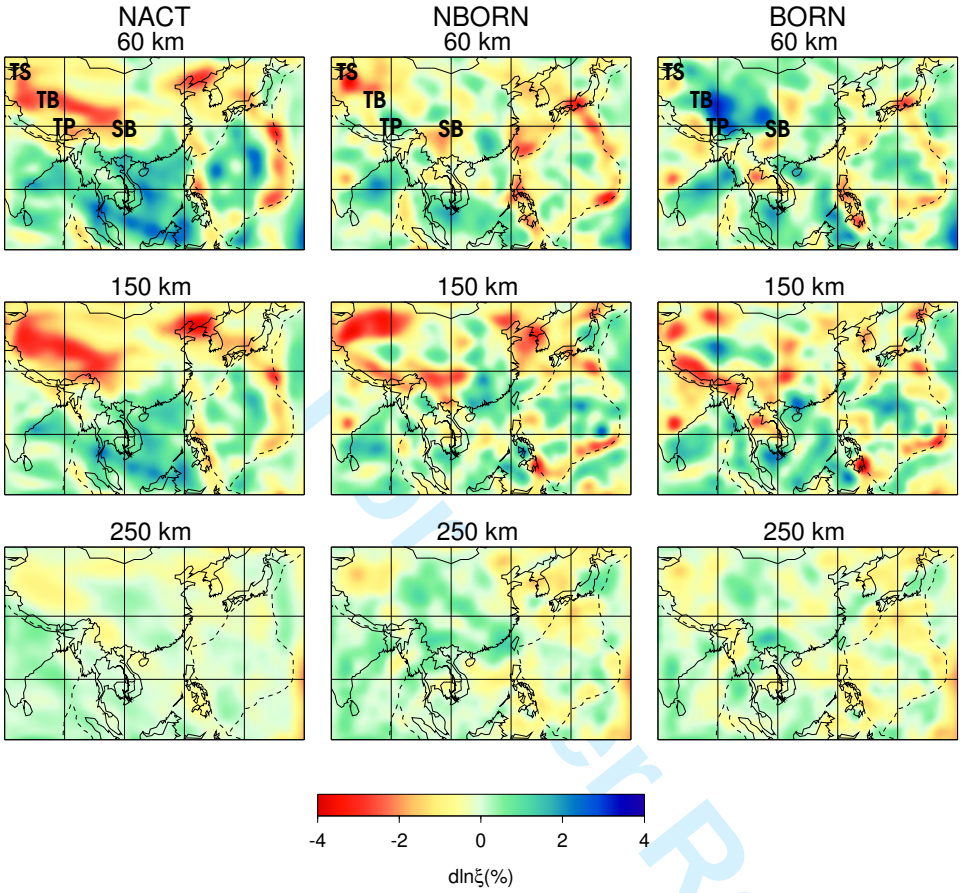

Figure S5. Same as figure S3 for ξ.

For Peer Review

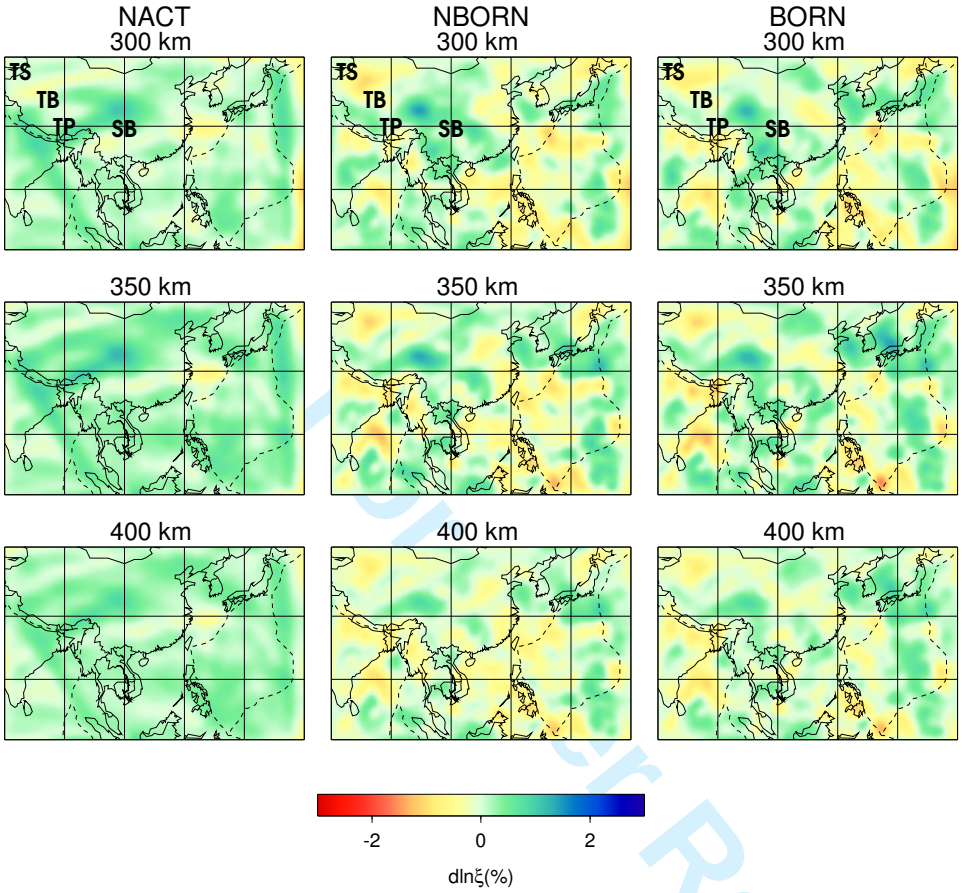

Figure S6. Same as figure S4 for ξ.

For Peer Review